Unveiling the Impact of Cross-Linking Redox-Active Polymers on Their Electrochemical Behavior by 3D Imaging and Statistical Microstructure Analysis

Marten Ademmer, Po-Hua Su, Lukas Dodell, Jakob Asenbauer, Markus Osenberg, André Hilger, Jeng-Kuei Chang, Ingo Manke, Matthias Neumann,* Volker Schmidt, and Dominic Bresser*

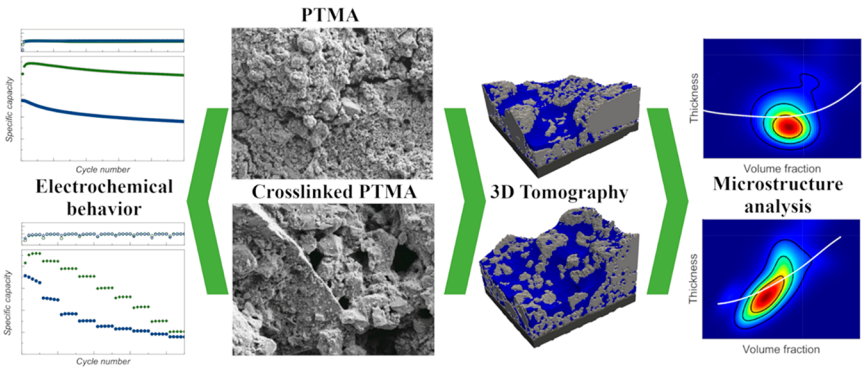

ABSTRACT: Polymer-based batteries offer potentially higher power densities and a smaller ecological footprint compared with state-of-the-art lithium-ion batteries comprising inorganic active materials. However, in order to benefit from these potential advantages, further research to find suitable material compositions is required. In the present paper, we compare two different electrode composites of poly(2,2,6,6-tetramethylpiperidinyloxy-4-yl methacrylate) (PTMA) and CMK-8, one produced with and one without cross-linking the PTMA. The influence of both approaches on the corresponding electrodes is comparatively investigated using electrochemical measurements and statistical 3D microstructure analysis based on synchrotron X-ray tomography. A particular focus is put on the local heterogeneity in the coating and how the cross-linking influences the interaction between PTMA and CMK-8. It is shown that cross-linked PTMA—compared to its non-cross-linked counterpart—exhibits a more heterogeneous microstructure and, furthermore, leads to better surface coverage of CMK-8, larger pores, and shorter transportation pathways through the latter. These changes improve the electrochemical properties of the electrode.

1. INTRODUCTION

Lithium-ion batteries (LIBs) are the dominating battery technology for small-scale applications such as portable electronics and large-scale applications including (hybrid) electric vehicles.[1,2] Nevertheless, important components such as graphite, the active material for the negative electrode, as well as nickel and cobalt, composed of $LiNi_{1-x-y}Mn_xCo_yO_2$ as the active material for the positive electrode, are considered critical concerning their long-term supply—especially in Europe.[3−5] To address these potential issues, alternative battery chemistries are needed that benefit from the use of more abundant elements and components. In fact, as not all applications eventually need the very high energy density provided by LIBs, sodium-ion batteries, for instance, are considered a viable (complementary) alternative.[6−8] Another alternative candidate is given by organic batteries, relying mostly on carbon—ideally derived from biomass—as an essentially unlimited resource.[9−11] One of the most studied organic active materials for the positive electrode is poly-(2,2,6,6-tetramethylpiperidinyloxy-4-yl methacrylate) (PTMA) owing its relatively high discharge/charge potential of about 3.6 V vs Li/Li^+ and excellent rate capability.[12−15] However, the dissolution of PTMA in organic electrolytes and the resulting continuous capacity loss remained an issue, hindering its practical application.[16−18] One strategy to overcome this issue relies on cross-linking the PTMA in order to decrease the solubility.[16,18−21] As a result, the PTMA-based electrodes showed higher capacities and substantially improved cycling

stability compared to the non-cross-linked analogues.[16,18,20,21] What remained unexplained somehow, though, is the substantially higher capacity recorded for the cross-linked PTMA despite the reduced radical concentration, the slower charge transfer kinetics, and the reduced swelling with the electrolyte.[18] These findings suggest that other factors play an important role in the achievable capacity—presumably factors that are dependent on the active material, i.e., the PTMA, itself. One such factor might be the accessibility of the redox active moieties—or, in other words, the spatial distribution of PTMA in the electrode and its overall microstructure. An appropriate methodology to quantitatively study the 3D electrode microstructure is the combination of tomographic imaging with image analysis, using methods of spatial statistics and mathematical morphology for investigating the resulting image data.[22,23] This allows for the computation of morphological microstructure descriptors which are, on the one hand, experimentally not accessible like the lengths of shortest transportation paths and, on the other hand, have a strong impact on effective physical properties such as effective ionic diffusivity.[24,25] In previous papers, this methodology has been widely used to study the morphology of differently manufactured electrodes in LIBs with $LiNi_{1-x-y}Mn_xCo_yO_2$ as the cathode active material,[26−29] where the use of machine learning opens new possibilities for an appropriate segmentation of image data, i.e., to reliably reconstruct the 3D microstructure from grayscale images. Recently, the influence of different binder materials on the morphology of classical PTMA-based electrodes has been studied for the first time,[30] where synchrotron X-ray tomography (XT) has been the method of choice to resolve the morphology of the 3D microstructure at the electrode scale.[31,32]

In the present paper, we use a combination of XT and statistical image analysis to investigate the impact of cross-linking PTMA on the electrochemical behavior. Following an optimization of the electrode composition by replacing part of the commonly used conductive carbon nanoparticles by a nanostructured mesoporous carbon, we conducted statistical image analysis based on a machine learning supported segmentation of image data, performed with the aid of the software Ilastik.[33] The results show that the cross-linking has a beneficial impact on the 3D electrode microstructure, leading to a pore network with improved connectivity properties and a larger interface between pores and solid material without significantly compromising the length of shortest transportation paths through the solid phase.

2. MATERIALS AND METHODS

2.1. Chemicals and Materials. The following reagents and solvents for the polymerization were used as received without additional purification: 4-methacryloyloxy-2,2,6,6-tetramethylpiperidine-*N*-oxyl (TEMPO-M, 98%, Sigma-Aldrich), 1-methoxy-2-methyl-1-trimethylsilyloxypropene (MTS, 97%, Alfa Aesar), tetra-*n*-butylammonium fluoride (TBAF, 1 M in tetrahydrofuran (THF), Alfa Aesar), THF (water-free, max 0.003% H_2O, >99.9%, stabilized with Ionol, VWR), and ethylene glycol dimethacrylate (stabilized with hydroquinone monomethyl ether for synthesis, Sigma-Aldrich).

2.2. PTMA Synthesis and Cross-Linking. The PTMA was synthesized via a group transfer polymerization as reported by Bugnon et al.[16] and depicted in Figure S1. The synthesis was performed in an argon-filled glovebox with an O_2 and H_2O content of less than 0.1 ppm. In brief, for the synthesis of the non-cross-linked PTMA (G-PTMA), 4.0 g of TEMPO-M was dissolved in 9.6 mL of THF under continuous stirring. After 5 min, 124 μL of MTS and 46 μL of TBAF were added dropwise into the solution. The polymerization was allowed to proceed for 40 h in the glovebox. Subsequently, 0.8 mL of methanol was added, and the resulting mixture was stirred for 5 min before pouring it dropwise into 100 mL of hexane provided in a round-bottom flask. The slightly pink, essentially white precipitate was collected as the final product. The remaining liquid phase was further stirred for 12 h to maximize the product yield by collecting the eventually remaining orange gel-like precipitate. The merged solid phases were dried at 60 °C under vacuum (< 10^{-2}mbar) for 12 h. The overall yield was about 80%. For the synthesis of the cross-linked PTMA (XG-PTMA), 0.0329 g of ethylene glycol dimethacrylate (EGDMA) was added at the very beginning to the 4.0 g of TEMPO-M dissolved in 9.6 mL of THF. All further steps remained the same.

2.3. Physicochemical Characterization. The successful synthesis of G-PTMA and cross-linked XG-PTMA was evaluated by means of Fourier-transform infrared (FTIR) spectroscopy (PerkinElmer Spectrum Two, attenuated total reflectance mode) and differential scanning calorimetry (DSC, Discovery series, TA Instruments) (Figure S2). The comparison of the FTIR spectra of XG-PTMA and the EGDMA cross-linker depicted in Figure S2a revealed that the characteristic absorption bands at 1293 and 3108 cm^{-1}, corresponding to the conjugated C−O bond and the alkene C−H bond in EGDMA, respectively, vanished in XG-PTMA, indicating the successful cross-linking. Moreover, the FTIR spectrum of XG-PTMA showed a small absorption band at 1637 cm^{-1}, which was absent for G-PTMA and appears to be characteristic for reacted EGDMA, as we also observed this in polymerized EGDMA (Figure S2b), which has been synthesized in the same way as (X)G-PTMA without adding the TEMPO-M monomer. In fact, also in poly-EGDMA the aforementioned bands at 1293 and 3108 cm^{-1} vanished—just as observed for XG-PTMA.

This was further corroborated by the DSC data (Figure S2c), revealing a slight increase of the glass transition temperature from 142 °C (G-PTMA) to 144 °C (XG-PTMA) owing to the decreased mobility of the polymer chains after cross-linking. Moreover, the determination of the number-average M_n and mass-average M_w of the molecular mass revealed higher values for XG-PTMA (20000 vs 48000 g mol^{-1} for M_n and 29000 vs 86000 g mol^{-1} for M_w), further corroborating the successful cross-linking via EGDMA. The molecular mass of the polymers was determined by gel permeation chromatography (GPC) using a multidetector Malvern Panalytical OmniSEC Resolve/Reveal system, equipped with a three-column setup (Viscotek D5000-D3000-D2000). The eluent was a 0.05 M LiBr solution in *N*,*N*-dimethylformamide (DMF) with a flux rate of 0.8 mL min^{-1} at 50 °C. The sample analysis was performed using a refractive index (RI) detector, accompanied by a UV detector, detectors for low-angle and right-angle light scattering (LALS and RALS), and a viscometer. The molecular mass was derived from the refractive index and the light scattering, utilizing a universal calibration method with one narrow poly(methyl methacrylate) (PMMA) standard, which was subsequently verified by analyzing an additional broad PMMA standard. Scanning electron microscopy (SEM) and energy-dispersive X-

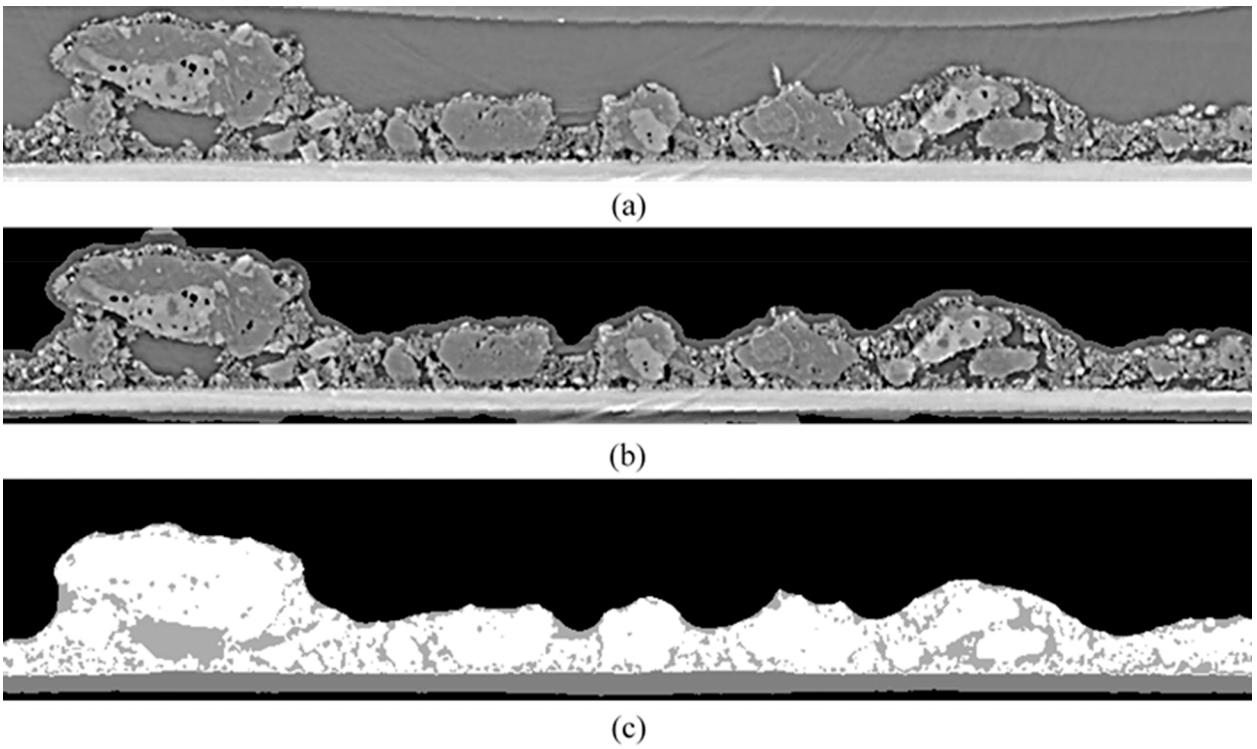

Figure 1. Exemplary slices of the sample with G-PTMA-CMK-8 from the XT image data (a), the mask before phase segmentation (b), and the final segmentation into the solid phase of the electrode coating (white), the current collector (dark gray), the pore space (light gray), and the background (black) (c).

ray spectroscopy (EDX) were performed using a ZEISS EVO MA 10 electron microscope equipped with an EDX detector (Oxford Instruments X-MaxN, 50 mm^2), applying acceleration voltages of 3 kV (SEM) and 10 kV (EDX). Nitrogen sorption measurements were performed using a Quadrasorb SI (Quantachrome), and the specific surface area and pore size distribution of the CMK-8 were determined by the Brunauer–Emmett–Teller (BET) and Barrett–Joyner–Halenda (BJH) method, respectively. Prior to these measurements, the samples were outgassed at 120 °C to remove potentially adsorbed water from the surface.

2.4. Electrode Preparation. A first batch of electrodes was prepared comprising only nanoparticulate conductive carbon (SuperC65, SC65, Imerys) as the electron-conducting additive. The electrode-active material was either G-PTMA or XG-PTMA, and the electrodes are termed G-PTMA-SC65 and XG-PTMA-SC65 (both 0.6–0.7 mg cm^{-2}), respectively. For the preparation of these electrodes, 54 wt % (X)G-PTMA, 41 wt % SC65, and 5 wt % sodium carboxymethyl cellulose (CMC, WALOCEL CRT, Dow Wolff Cellulosics) were mixed by manual grinding before adding deionized water. The resulting slurry was stirred for 12 h before casting it with a laboratory-scale doctor blade on an aluminum foil serving as the current collector (wet film thickness: 120 μm). The thus-prepared electrodes were initially dried at 80 °C for 6 h before punching disc-shaped electrodes with a diameter of 12 mm. These electrodes were further dried under a vacuum ($<10^{-2}$ mbar) at room temperature for 3 h and at 120 °C for 12 h.

For the second batch of electrodes, the conductive additive SC65 was partially replaced with CMK-8 (ACS Material). Initially, 60 mg of (X)G-PTMA was manually mixed with 40 mg of CMK-8 in 0.5 mL of 2-butoxyethyl acetate (BCA) to enhance the contact between the two components. To fully dissolve the PTMA, the temperature of the mixture was increased to 80 °C and maintained at this temperature for 4 h, before further increasing it to 160 °C and maintaining it at this further elevated temperature for 12 h to completely evaporate the BCA. The thus-obtained powder was additionally dried at 80 °C under vacuum ($<10^{-2}$ mbar) overnight. The subsequent electrode preparation was the same as for the first batch of electrodes, except the resulting difference concerning the electrode composition, which was 54:36:5:5 (X(G)-PTMA/CMK-8/SC65/CMC) by weight. The resulting electrodes were termed XG-PTMA-CMK-8 and G-PTMA-CMK-8 (both 1.3–1.6 mg cm^{-2}).

2.5. Cell Assembly and Electrochemical Characterization. Three-electrode Swagelok-type cells were assembled in an argon-filled glovebox (O_2< 0.1 ppm and H_2O < 0.1 ppm). Lithium metal foil (Honjo) served as counter and reference electrode, and the electrodes were separated by glass microfiber sheets (Whatman, GF/A). The separator between the working and counter electrode was drenched with 120 μL of the electrolyte, i.e., 1 M $LiPF_6$in a 1:1 volume mixture of ethylene carbonate (EC) and dimethyl carbonate (DMC), purchased from UBE. The cells were subjected to galvanostatic cycling using a Maccor 4000 battery tester. The testing temperature was kept constant at 20 °C by placing the cells in a climatic chamber (Binder). The cutoff voltages were set to 3.0 and 4.0 V vs Li^+/Li. Prior to the cycling, the cells were allowed to rest for 12 h. The given values for the specific current, ranging from 25 mA g^{-1} to 10 A g^{-1}, refer to the mass of the active material.

2.6. Synchrotron X-ray Tomography. To further characterize and compare the electrodes, prepared as described in Section 2, in terms of their morphology at the microscale, three-dimensional (3D) images were captured using XT. The

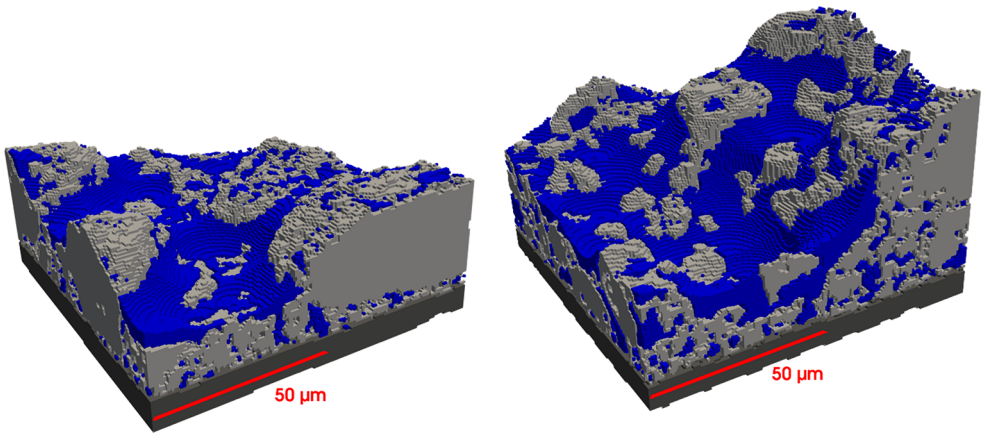

Figure 2. 3D rendering of image data of the electrode based on G-PTMA-CMK-8 (left) and XG-PTMA-CMK-8 (right), segmented into the solid phase of the electrode coating (light gray), the current collector (dark gray), and the pore space (blue).

synchrotron tomography experiments were performed at the P05 beamline at PETRA III (DESY, Germany).[34] The samples were exposed to a synchrotron energy of 20 keV. During the tomography, the sample was continuously rotated over 180°, while 3001 projections were acquired with an exposure time of 0.3 s each. The sample rotation axis had a distance of 15 mm to the $CdWO_4$ scintillator screen, resulting in a small amount of phase contrast. The scintillator projection image was magnified with a 10× microscope optic and then captured using a KIT CMOS camera yielding a pixel size of 0.64 μm.

For the reconstruction of the tomography data, the filtered back-projection based software developed at DESY was used.[35] After reconstruction, an additional total variation denoising filter was applied.[36] The resulting 3D image data are the basis for the microstructure characterization.

3. RESULTS

3.1. 3D Microstructure Characterization: Tomographic Imaging. Prior to the characterization of the microstructure by statistical analysis of the 3D image data representing the electrode microstructure, some preprocessing steps were required. First, the 3D images were rotated to align them with the coordinate system of the sampling window. Next, a global threshold and a morphological opening using a sphere of radius 5 voxels as structuring element were applied to roughly separate the aluminum foil of each sample from the solid phase, pores, and background. Here and in the following, solid phase means the solid phase of the coating. Based on this preliminary foil segmentation, the polynomial approach described by Westhoff et al.[37] was used to straighten the sample, i.e., to align the aluminum foil such that it is parallel to the $x-y$ plane. Note that a final segmentation of the aluminum foil was obtained by means of random forests, as described below. After this alignment, additional steps were performed to determine a mask, in which the electrode was contained, and subsequently to create a segmentation separating solid phase, pore space, and aluminum foil. As shown in Figure 1a, there were large variations in the grayscale values in that part of the image, which we would visually attribute to the solid phase. Because of this variation it was not possible to classify a voxel as solid phase, pore space, or aluminum merely based on its grayscale value. In the following, an appropriate three-step procedure is proposed to obtain an accurate segmentation of the data. In short, the Sobel edge detection operator[38] in conjunction with a cluster analysis was used to create a mask of the electrode, i.e., to roughly separate the electrode structure from the surrounding background. From this, a morphological closing was used to determine the boundaries of the sample, and finally, a random forest classifier was used to create the final segmentation. To determine the mask, the Sobel edge detection operator was applied to the aligned grayscale image data, creating gradient images. Those images were binarized by global thresholding to identify the interfaces between pores and solid. The threshold was chosen in such a way that most of the edges form a connected phase in 3D. A cluster analysis was used to find all of the connected components in the complement of this edge phase. The two largest clusters were the two regions above the coating and below the aluminum foil, i.e., the background of the sample. To remove artifacts resulting from the edge detection, a morphological closing with a sphere of radius 11 voxel as a structuring element was applied to the background. The mask, which contains the electrode structure, was finally given by a complement of the background. A 2D example slice of the mask for the sample without cross-linking is shown in Figure 1b. In the next step, the aluminum foil, the solid phase, and the pore space had to be separated from one another within the mask. As mentioned before, simply assigning each voxel to one of the three phases using global thresholds was not appropriate. Therefore, two random forest classifiers[39] were trained using Ilastik[33] based on hand-labeled training data. First, a random forest was trained that separated the aluminum foil from its complement. Subsequently, a second random forest was trained classifying all voxels, not already determined to be aluminum foil, as either pores or solid. This approach was convenient, as the number of hand-labeled areas needed to create an accurate segmentation was reasonably small. An example of a hand-labeled 2D slice is shown in Figure S3. Thus, we obtained 3D image data, where the voxels were classified as aluminum foil, solid phase, or void, i.e., pores classified by the random forest or voxels outside the mask. To distinguish between inner pores, which are not necessarily identical with the pores determined by the random forest, we used the rolling ball algorithm with a radius of 20 voxels as described by Charry et al.[40] In Figure 1c, an example of the resulting segmentation is shown, on the basis of which the microstructure analysis described in the next section was performed.

Table 1. Global Descriptors Quantifying the Microstructure of the G-PTMA-CMK-8 and XG-PTMA-CMK-8 Electrodes

	vol fraction solid phase (%)	thickness (μm)	surf area per unit vol (μm^{-1})	mean geodesic tortuosity (pore space)	mean geodesic tortuosity (solid phase)
G-PTMA-CMK-8	76	22.4	0.274	1.24	1.03
XG-PTMA-CMK-8	65	26.7	0.294	1.11	1.05

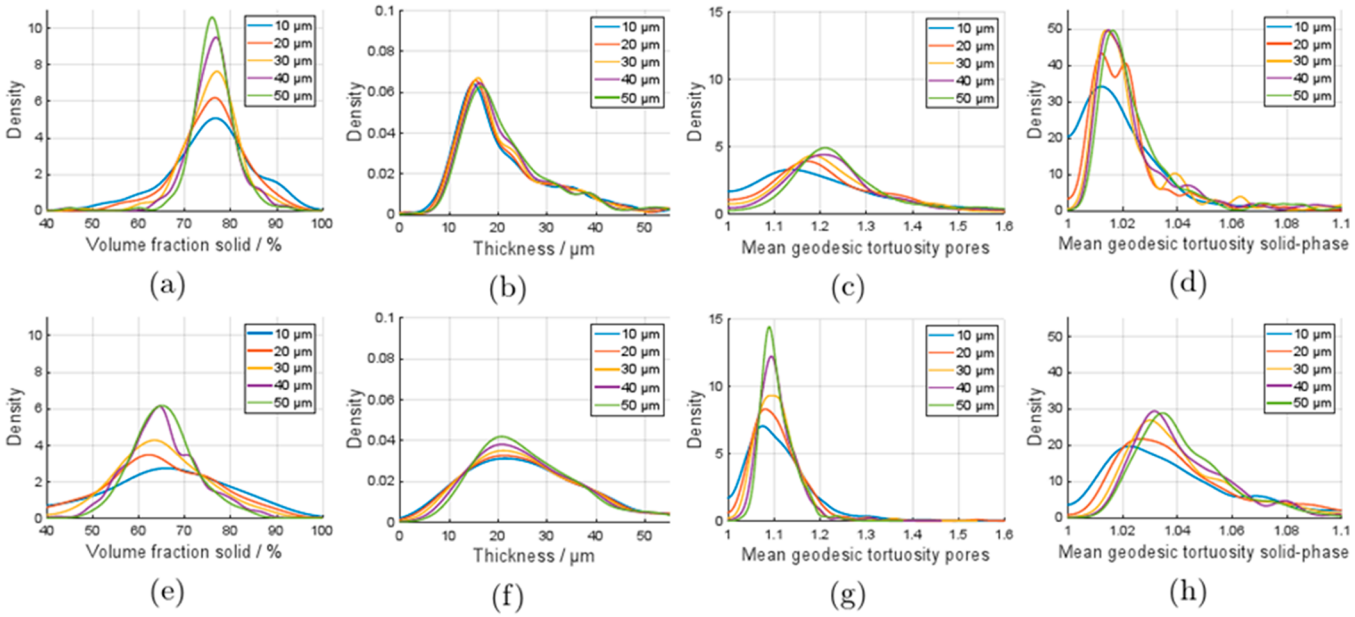

Figure 3. Univariate distributions of local microstructure descriptors (volume fraction, thickness, mean geodesic tortuosity pores, and mean geodesic tortuosity solid phase) of the G-PTMA-CMK8 electrode (top row) and the XG-PTMA-CMK8 electrode (bottom row) computed from cutouts with increasing window sizes.

3.2. 3D Microstructure Characterization: Statistical Image Analysis. The separation of solid phase, pore space, and aluminum foil in the 3D image segmentation as described in the previous section enabled us to characterize the microstructure of the electrodes by means of statistical image analysis. For this purpose, global as well as local microstructure descriptors and pairwise interdependencies between them are discussed for each sample. Methodologically similar microstructure characterizations are presented in refs 30 and 41 for differently manufactured PTMA-based electrodes and paper-based materials, respectively.

To begin with, the microstructure descriptors for both samples were to be computed. A uniform hexahedral grid of points, with a distance of 50 μm between neighboring grid points, was superimposed over each sample in $x-y$ direction, i.e., the plane parallel to the electrode coating and aluminum foil. Each point was the center of a sampling window for the computation of local microstructure descriptors. These non-overlapping sampling windows extended over the complete sample thickness or, more precisely, from the aluminum foil to the opposite boundary in z direction. The edges of these sampling windows in the $x-y$ direction were increased from 10 to 50 μm in 10 μm steps. This led to 189 sampling windows across the electrode based on G-PTMA-CMK-8 and 330 across the XG-PTMA-CMK-8 electrode. In Figure 2, a 3D rendering of a cutout of 100 μm is shown to give a visual impression of the sample differences and local variability of the samples themselves. Note that the computed descriptors of such a sampling window are the averaged results computed for the respective local sampling window. Additionally, note that for the descriptors considered in the present paper, the mean computed across all sampling windows with an edge length of 50 μm is equal to the mean of the complete sample. These mean values are global microstructure descriptors and are summarized in Table 1. As descriptors, we considered the volume fraction of the solid phase, the electrode thickness, the surface area per unit volume (SAV) of the solid phase, and the mean geodesic tortuosities of the solid phase and the pore space. For a given point in the $x-y$ plane, its pointwise thickness was defined as the distance between the first and the last voxel (with the same $x-y$ coordinates) of the electrode in the z direction. The thickness of a predefined sampling window was then given as the average value of all pointwise thicknesses for the points within the sampling window under consideration. To compute the surface area from voxelized image data, we used the method described previously.[42] Mean geodesic tortuosity quantifies the length of transportation paths.[24,43] It was defined as the mean length of the shortest transportation paths starting from the aluminum foil intersected with this cutout and reaching the opposite boundary of the electrode through the considered material phase. Note that these paths were allowed to leave the given local sampling window to avoid edge effects.

Considering the global microstructure descriptors in Table 1, we observed that the cross-linked sample was thicker and exhibited a smaller volume fraction of the solid phase, i.e., a higher porosity. The increased porosity is most likely the reason for the smaller mean geodesic tortuosity of the pore space in the cross-linked case, while the mean geodesic tortuosity of the solid phase was close to 1 in both cases. Moreover, the specific surface area per unit volume was 7% larger for XG-PTMA-CMK-8 compared to G-PTMA-CMK-8.

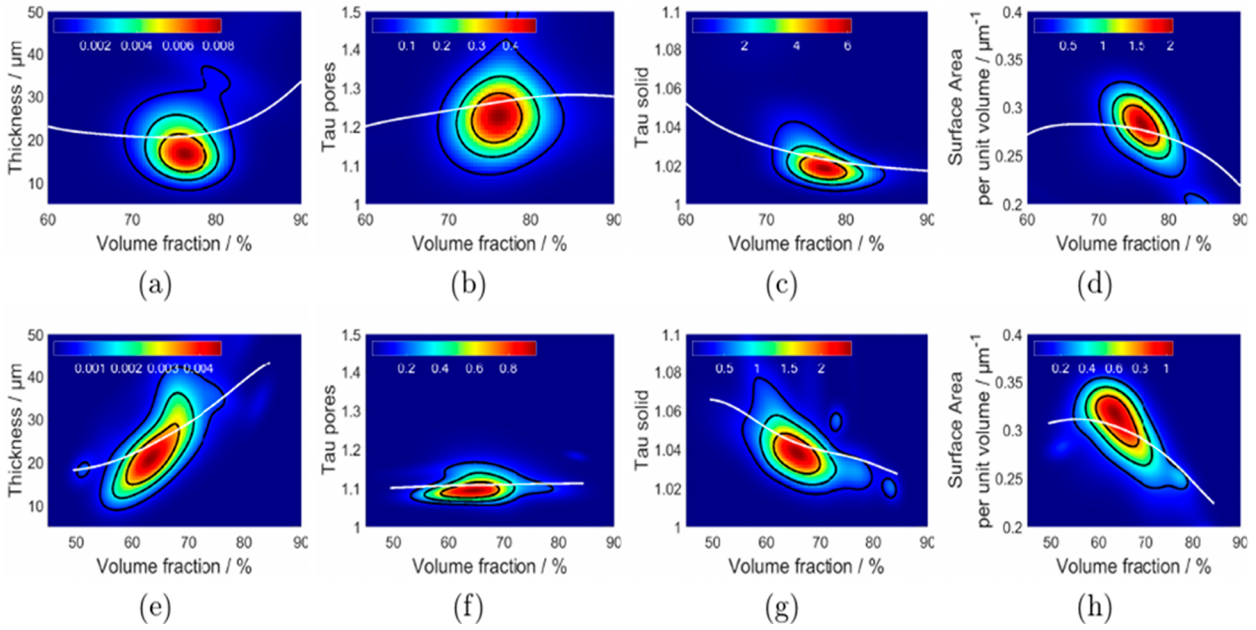

Figure 4. Bivariate distributions of pairs of local microstructure descriptors (thickness, τ pores, τ solid phase, and surface area) of G-PTMA-CMK8 (top row) and XG-PTMA-CMK8 (bottom row) computed from cutouts with a size of 50 μm. The bivariate probability density functions are visualized as heat maps, where the white line represents the (conditional) mean value for given local volume fractions of the polymer phase. The black contour lines are the 25%, 50%, and 75% quantiles.

Note that similar to the observations in ref 30 there seems to be a negative correlation between volume fraction and SAV of the solid phase for volume fractions above 60% because the XG-PTMA-CMK-8 sample had a slightly higher global SAV compared to the G-PTMA-CMK-8 electrode (0.294 μm^{-1} vs 0.274 μm^{-1}). A larger SAV can be advantageous, as it quantifies the amount of boundary at which the electrolyte and the solid phase can interact. We will come back to this relationship when discussing the interdependence of local microstructure characteristics in detail.

Besides the global morphology of electrode microstructures, we also quantitatively investigated local heterogeneities. Figure 2 shows the heterogeneity of both samples at the microscale, while G-PTMA-CMK-8 seemed to be more homogeneous than XG-PTMA-CMK-8. In particular, comparing these cutouts, larger variations in thickness and volume fraction of the solid phase were observed for the coating of the XG-PTMA-CMK-8 sample. These visual impressions were confirmed by our statistical analysis (see the distributions of the local volume fraction of the solid phase in Figure 3a,e). Even though the G-PTMA-CMK-8 sample exhibited relatively strong heterogeneities, where variations of volume fraction of the solid phase were especially pronounced for the smaller sampling windows, the XG-PTMA-CMK-8 sample was considerably more heterogeneous. Especially for sampling windows with an edge length of 10 μm the variations of volume fraction of the solid phase were considerably larger. While some sampling windows had a volume fraction below 40%, it was above 90% in other sampling windows. As expected, this gap became smaller for increasing sizes of the sampling windows. The distributions of local SAV, visualized in Figure S4, show a similar behavior to the distributions of local volume fractions, where a larger variability was observed for XG-PTMA-CMK-8.

Similar observations were made with regard to the distributions of the local thickness of both samples shown in Figure 3b,f. The decrease of variability for an increasing window size was much less pronounced compared to that of local volume fractions for both samples. The distributions of local thickness were considerably wider across all sizes of sampling windows for XG-PTMA-CMK-8. Even for sampling windows with an edge length of 50 μm, the local thickness of XG-PTMA-CMK-8 varied more than the local thickness for sampling windows of G-PTMA-CMK-8 with an edge length of 10 μm. An interesting observation, however, was that while the local thickness distributions of XG-PTMA-CMK-8 were nearly symmetrical, they were clearly positively skewed for G-PTMA-CMK-8. Another important observation was the difference in mean thickness between both samples. Because the wet films on the aluminum foil exhibited the same thicknesses before drying, the difference in terms of thickness was apparently a result of the drying process. Furthermore, as both material compositions consisted of the same weight percentage of solid materials, we conclude that the drying created larger pores in the coating of the XG-PTMA-CMK-8 sample. This matches the visual impression and is in good accordance with the larger volume fraction of the solid phase observed for the G-PTMA-CMK-8 electrode.

The local distributions of mean geodesic tortuosities of the pore space and the solid phase are shown in Figures 3c,g and 3d,h, respectively. Because of the lower values of local porosity of G-PTMA-CMK-8, it is not surprising that the mean geodesic tortuosity of the pore phase of this electrode was larger and varied more than that of the XG-PTMA-CMK-8 electrode. For the mean geodesic tortuosity of the solid phase, the opposite was observed. The generally higher volume fraction of the solid phase in the G-PTMA-CMK-8 sample led to shorter transportation paths in the solid phase, thereby decreasing the mean geodesic tortuosity.

For the considered electrode materials, a more interesting quantity is the mean geodesic tortuosity of the pore phase because the supply of electrons in the solid phase is rarely a

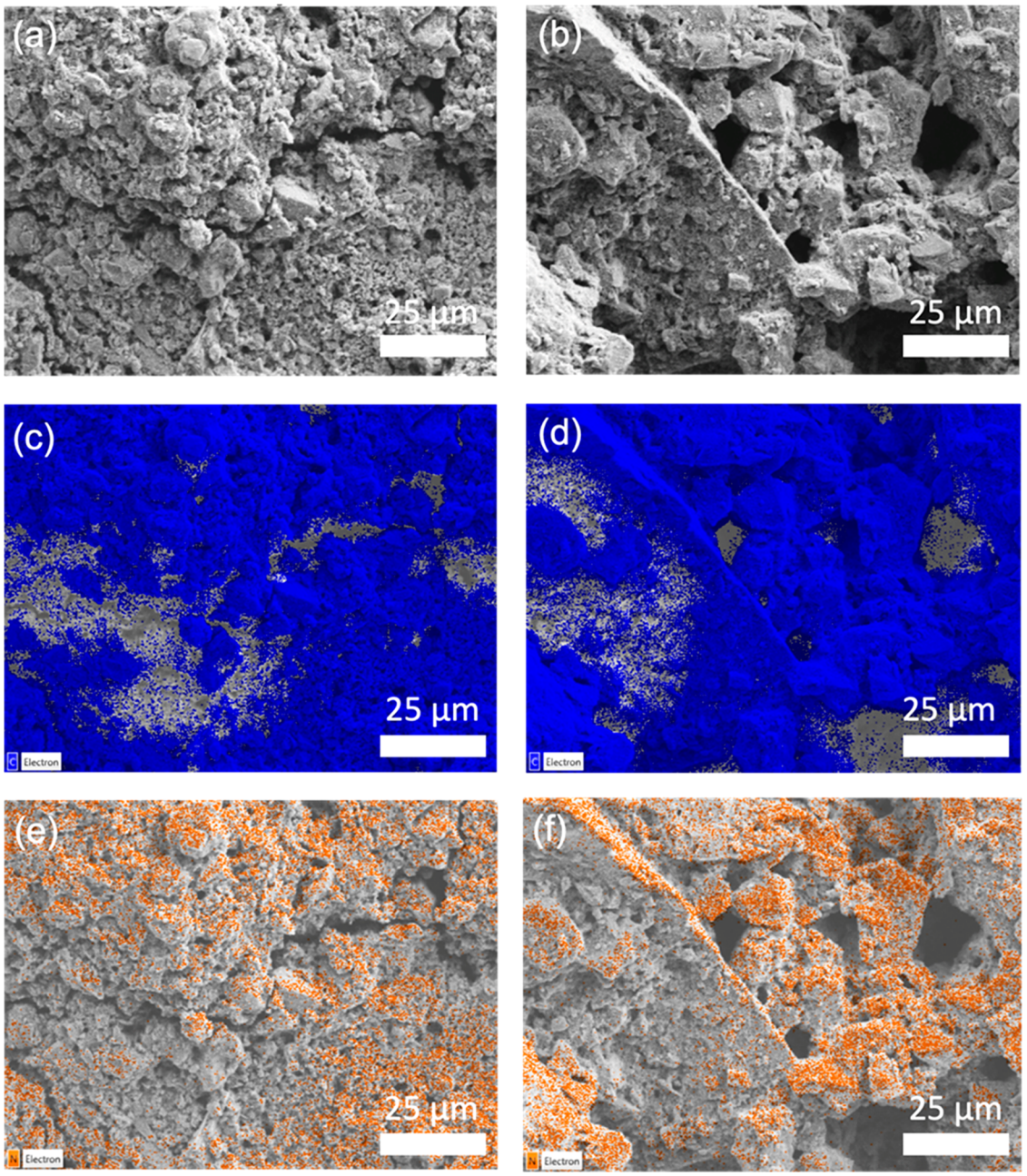

Figure 5. SEM micrographs of G-PTMA-CMK-8 (a) and XG-PTMA-CMK-8 (b) electrodes and the corresponding EDX mappings of carbon (in blue) and nitrogen (in orange) for G-PTMA-CMK-8 (c, e) and XG-PTMA-CMK-8 (d, f).

limiting factor regarding the performance of the cell. XG-PTMA-CMK-8 not only had a significantly lower mean value with 1.11 compared to the 1.24 of G-PTMA-CMK-8, but additionally, just a few of the considered local sampling windows had a mean geodesic tortuosity exceeding 1.2. On the other hand, some windows even reached 1.5 in the case of G-PTMA-CMK-8. It is important to note that these differences were especially significant in this context as the samples were rather thin in comparison to the typical cluster size in the solid phase. In other words, because many clusters of the solid phase exhibited the same thickness as the complete coating, the amount of obstructions decreased significantly at a certain distance from the start, leading to many paths being nearly straight after the first few voxels. Therefore, it is to be expected that the length of the shortest paths would increase more slowly with increasing sample thickness, decreasing the mean geodesic tortuosity of both samples and additionally widening the gap between them.

On the other hand, because many of these clusters directly connect the foil with the opposite boundary, the values of mean geodesic tortuosity of the solid phase were nearly 1 for both samples. Even in the extreme cases, in which the mean geodesic tortuosity through the solid phase reached values of up to 1.1 for the XG-PTMA-CMK-8 electrode, these values were still smaller than the global mean geodesic tortuosity of the pore phase.

Finally, to quantify the interdependence between pairs of local microstructure descriptors, we consider the bivariate distributions of local porosity and each of the other local microstructure descriptors considered in the present paper.

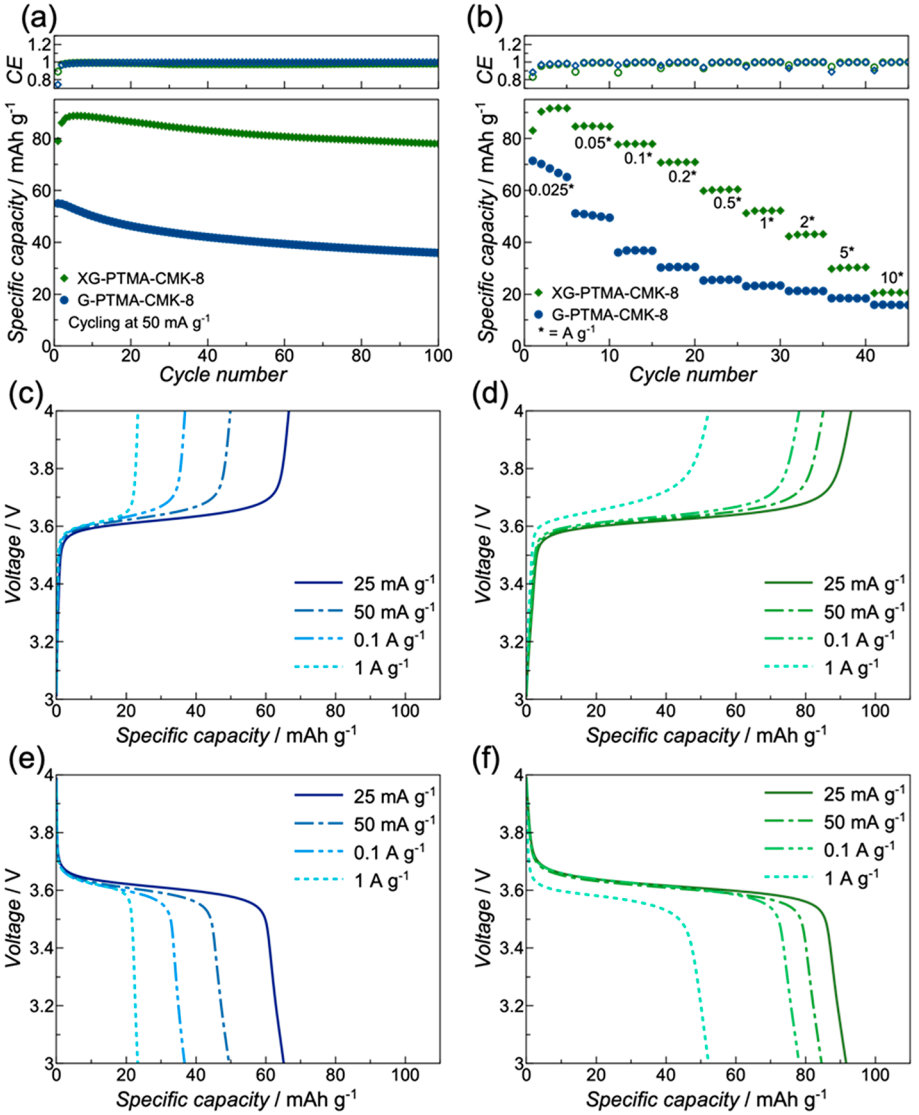

Figure 6. Galvanostatic cycling of G-PTMA-CMK-8 (blue) and XG-PTMA-CMK-8 electrodes (in green). Comparison of the constant current cycling at 50 mA g^{-1} (a) (rate capability test at varying specific currents from 0.025 to 10 A g^{-1} (b); exemplary charge (c, d) and discharge profiles (e, f) of G-PTMA-CMK-8 (c, e) and XG-PTMA-CMK-8 (d, f) electrodes at specific currents ranging from 25 mA g^{-1} to 1 A g^{-1}.

In general, the larger heterogeneity of XG-PTMA-CMK-8 was also reflected in the bivariate distributions. However, the only clear difference between the samples with respect to bivariate distributions was that there was a stronger relationship between thickness and volume fraction of the solid phase for XG-PTMA-CMK-8 compared to G-PTMA-CMK-8 (see Figure 4a,e). The other bivariate distributions showed similar trends in both cases. Nevertheless, an interesting observation was made with regard to the bivariate distribution of the volume fraction and the mean geodesic tortuosity of the pore phase. More precisely, there did not seem to be a correlation between both microstructure descriptors, as seen in Figure 4b,f. This was true for both samples and was especially surprising taking into account that as discussed before, a smaller volume fraction, in general, leads to shorter transportation paths in the pore space. Furthermore, Figure 4c,g shows that, as expected, the volume fraction and mean geodesic tortuosity of the solid phase were clearly negatively correlated. This different behavior of the shortest paths in the pore space and the solid phase can be explained by considering two opposing influences of local thickness on the local mean geodesic tortuosity of the pore phase. In particular, the shortest transportation paths in the pore phase often circumvent the first obstacle, i.e., the first cluster of the solid phase they meet and from there go directly to the separator. Just considering this effect, a negative correlation between local thickness and local mean geodesic tortuosity should be expected since, in thicker areas of the samples, the segment where the path circumvents those clusters is smaller. On the other hand, the effect that thickness negatively correlates with porosity would lead to a positive correlation between local thickness and local mean geodesic tortuosity of the pore phase. Our results, in which no correlation was visible, indicate that these two effects were balanced for the electrodes considered in this paper.

Finally, note that in Figure 4d,h a negative correlation between the surface area per unit volume and the volume fraction of the solid phase, also mentioned when discussing the global microstructure descriptors, was observed. Moreover, the mean values of SAV conditioned on the local volume fraction

showed a maximum at approximately 60%. This coincides with the findings reported by Neumann et al.[30]

3.3. Electrochemical Characterization. First, we investigated the electrochemical behavior of G-PTMA and XG-PTMA in a standard electrode configuration using SC65 as the electron conductive additive. The results are presented in Figure S5, revealing a superior specific capacity for the cross-linked XG-PTMA-SC65 electrodes—in line with previous papers on the impact of cross-linking.[16,18,20,21] However, the capacity remained generally rather low at about 60 mAh (XG-PTMA-SC65) and 50 mAh g^{-1} (G-PTMA-SC65). Thus, we replaced part of the nanoparticulate SC65 with nanostructured mesoporous CMK-8, following previous studies on such material as conductive additive, which showed a highly beneficial impact of such carbon.[44−46] The basic characterization of CMK-8 is provided in Figure S6, revealing a particle size of several micrometers with frequently more than 10 μm (Figure S6a), a specific surface area of 574 m^2 g^{-1} (Figure S6b), and a mean pore size of around 22 Å (Figure S6c). SEM micrographs of the resulting electrodes, i.e., G-PTMA-CMK-8 and XG-PTMA-CMK-8, are displayed in Figures 5a and 5b, respectively. Generally, the G-PTMA-CMK-8 electrodes showed less of the relatively large holes in the electrode coating layer, while the XG-PTMA-CMK-8 electrode morphology largely resembled the morphology of the CMK-8 particles (cf. Figure S6a,b). This indicates that cross-linking the PTMA yielded a better surface coverage of the CMK-8 conductive carbon, which was confirmed by the EDX mapping presented in Figure 5c−f and, in particular, the EDX mapping of nitrogen in Figure 5e,f. In fact, in the case of G-PTMA-CMK-8 (Figure 5e), the PTMA appeared to be well distributed across the overall electrode, while it was detectable only on the larger "edgy" particles in the case of XG-PTMA-CMK-8 (Figure 5f). The more intimate contact with the CMK-8 might be beneficial for the performance of the electrodes following previous studies reporting the need for an intimate mixing of PTMA and nanosized carbons.[20,21]

To investigate this, the G-PTMA-CMK-8 and XG-PTMA-CMK-8 electrodes were subjected to galvanostatic cycling with a lithium−metal counter electrode (Figure 6). While both electrodes showed increased capacities compared to the CMK-8-free G-PTMA-SC65 and XG-PTMA-SC65 electrodes (Figure S5) with 54 mAh g^{-1} (G-PTMA-CMK-8) and 88 mAh g^{-1} (XG-PTMA-CMK-8), the capacity increase was more pronounced for XG-PTMA-CMK-8 (Figure 6a). In the latter case, also the capacity retention was much greater with 89% compared to only 65% for the non-cross-linked PTMA after 100 cycles, which underlines the beneficial impact of cross-linking concerning the solubility in the liquid organic electrolyte.[19] The rate capability of the two different electrodes was evaluated as well, and the results are presented in Figure 6b. In general, XG-PTMA-CMK-8 provided higher specific capacities at all specific currents with, e.g., 91 vs 71 mAh g^{-1} at 25 mA g^{-1} and 52 vs 23 mAh g^{-1} at 1 A g^{-1}. Nonetheless, the gap between the two different electrodes narrowed at elevated specific currents, suggesting that especially at very high specific currents of several A g^{-1} the positive impact of the cross-linking vanishes. The comparison of the discharge/charge profiles (Figure 6c−f) revealed that for G-PTMA-CMK-8 (Figure 6c,e) there is essentially only a shortening of the voltage plateau, while for XG-PTMA-CMK-8 (Figure 6d,f) the same behavior was observed for only a specific current up to 0.1 A g^{-1}. When the current was further increased, additionally a significant increase in polarization was observed—still yielding a higher specific capacity, though. In fact, the more pronounced increase in polarization is even more evident from the comparison of further increased specific currents (Figure S7a−d), resulting in a greater voltage hysteresis compared to that of G-PTMA-CMK-8 (Figure S7e,f). This observation is in line with the preferential CMK-8 surface coverage of the cross-linked PTMA, leading to a higher polarization owing to its electronically insulating nature.

4. DISCUSSION

The combination of 3D imaging with statistical microstructure analysis further elucidated the differences between G-PTMA-CMK-8 and XG-PTMA-CMK-8 in terms of their electrochemical behavior. Differences with regard to the spatial distribution of pores and PTMA were also visible in the 3D image data and could be quantified by the selected microstructure descriptors. In particular, statistical analysis of image data revealed that the XG-PTMA-CMK-8 electrode was considerably more heterogeneous. This can be attributed to the fact that the PTMA in the XG-PTMA-CMK-8 electrode seems to better cover the CMK-8, leading to a higher number of large clusters of the solid phase. Moreover, it is shown that the local volume fraction of the solid phase and the local sample thickness positively correlate (Figure 4a,e), meaning that the local thickness of the coating is highly dependent on the presence of clusters of the solid phase. Compared to XG-PTMA-CMK-8, the electrode comprising G-PTMA-CMK-8 was thinner on average, and the solid phase was more homogeneously distributed with only a relatively small number of large clusters. Thus, the sample with XG-PTMA-CMK-8 exhibited not only a higher porosity but also larger pores. This results in considerably different behavior of the considered samples regarding mean geodesic tortuosity, quantifying the length of shortest transportation paths. First, the transportation paths through the pore phase of the XG-PTMA-CMK-8 electrode were significantly shorter compared to those of G-PTMA-CMK-8. Second, the surface area per unit volume was larger for XG-PTMA-CMK-8 than for G-PTMA-CMK-8; i.e., XG-PTMA-CMK-8 had a larger interface at which the electrolyte in the pores can interact with the solid phase and, thus, with the PTMA. Both properties are beneficial for the discharge/charge performance of the electrode.

Moreover, it is reasonable to presume that this larger SAV amplified the beneficial effect of the improved surface coverage of CMK-8 by the cross-linked PTMA. Note that even though one could expect the mean geodesic tortuosity of the solid phase to get worse with cross-linked PTMA due to the higher porosity, only a negligibly small increase of mean geodesic tortuosity was observed.

These changes of the 3D microstructure are presumably one of the factors leading to another observation made during the experiments, namely the vanishing impact of cross-linking for especially high specific currents. As discussed above, the microstructure of the sample with XG-PTMA-CMK-8 had a less restricting pore phase regarding the shortest transportation paths, thereby having a positive effect on the rate capability of this sample. However, the current flow is, of course, still influenced by the microstructure. The impact of these restrictions increased with an increasing specific current. For very large specific currents, it is reasonable to assume that the whole pore network becomes a limiting factor to charge transfer, such that the differences between both samples

become negligibly small, thereby negating the advantage of cross-linking.

5. CONCLUSIONS

In the present paper, we were able to show the positive effects of cross-linking PTMA on the electrochemical performance. For this purpose, two electrodes, one with ordinary PTMA and one with cross-linked PTMA, were compared based on their electrochemical characteristics and the 3D morphology of their microstructures. These electrodes were experimentally investigated by means of SEM, EDX mapping, and galvanostatic cycling. Moreover, statistical image analysis was performed to quantify the electrode microstructures based on 3D image data, which were obtained by XT. Compared to the spatial distribution of the non-cross-linked PTMA in the G-PTMA-CMK-8 electrode, the material in the electrode based on the cross-linked PTMA aggregates to larger clusters and larger pores emerge across the coating during the drying process. This leads to the morphology of the XG-PTMA-CMK-8 sample closely resembling the morphology of the conductive additive CMK-8. By resolving the 3D morphology using XT, we were additionally able to show that the large number of agglomerates in the XG-PTMA-CMK-8 sample leads to a morphology, where the lengths of the shortest transportation paths through the pore space are significantly smaller compared to those of G-PTMA-CMK-8.

Furthermore, based on the galvanostatic cycling of the samples, we were able to show that the electrochemical properties of the sample with cross-linking are clearly preferable, with a larger capacity, larger capacity retention after 100 cycles, and higher rate capability. These improvements are presumably amplified by the microstructure differences because the shorter transportation paths through the pore space and the larger interface between electrolyte and solid phase facilitate a homogeneous discharge/charging of the electrodes. These findings lead to a better understanding of the positive influence of cross-linking the PTMA and, more generally, provide a first impression on how the electrochemical properties of such polymer electrodes are influenced by the underlying microstructure. Future studies may build up on these results and target the investigation of, for instance, redox-active polymer-based electrodes with further advanced electrode architectures and compositions, including novel conductive additives and active material ratios of at least 90%, as well as other (novel) polymer chemistries, thus ideally providing some guidance toward the realization of high-performance polymer electrodes with sufficiently high areal capacities for practical applications. In fact, ensuring high electronic conductivity and facile accessibility of the electrolyte to all redox-active moieties will be key if such materials reach a commercially relevant level beyond thin-film battery applications.

AUTHOR INFORMATION

Corresponding Authors

Dominic Bresser − *Helmholtz Institute Ulm (HIU), 89081 Ulm, Germany; Karlsruhe Institute of Technology (KIT), 76021 Karlsruhe, Germany;* orcid.org/0000-0001-6429-6048; Email: dominic.bresser@kit.edu

Matthias Neumann − *Institute of Stochastics, Ulm University, 89069 Ulm, Germany*; Email: matthias.neumann@uni-ulm.de

Authors

Marten Ademmer − *Institute of Stochastics, Ulm University, 89069 Ulm, Germany*

Po-Hua Su − *Helmholtz Institute Ulm (HIU), 89081 Ulm, Germany; Karlsruhe Institute of Technology (KIT), 76021 Karlsruhe, Germany*

Lukas Dodell − *Institute of Stochastics, Ulm University, 89069 Ulm, Germany*

Jakob Asenbauer − *Helmholtz Institute Ulm (HIU), 89081 Ulm, Germany; Karlsruhe Institute of Technology (KIT), 76021 Karlsruhe, Germany*

Markus Osenberg − *Institute of Applied Materials, Helmholtz-Zentrum für Materialien und Energie, 14109 Berlin, Germany*

André Hilger − *Institute of Applied Materials, Helmholtz-Zentrum für Materialien und Energie, 14109 Berlin, Germany*

Jeng-Kuei Chang − *Department of Materials Science and Engineering, National Yang Ming Chiao Tung University, Hsinchu 30010, Taiwan; Department of Chemical Engineering, Chung Yuan Christian University, Taoyuan 32023, Taiwan*

Ingo Manke − *Institute of Applied Materials, Helmholtz-Zentrum für Materialien und Energie, 14109 Berlin, Germany;* orcid.org/0000-0001-9795-5345

Volker Schmidt − *Institute of Stochastics, Ulm University, 89069 Ulm, Germany*

Author Contributions

M.A. and P.-H.S. contributed equally to this work.

Notes

The authors declare no competing financial interest.

ACKNOWLEDGMENTS

All authors are grateful to the German Research Foundation (DFG) for funding their research projects within the framework of SPP 2248 "Polymer-based Batteries" (BR 5752/4-1, MA 5039/7-1, SCHM 997/39-1). The work of M.N. was funded by the German Research Foundation (DFG) under Project ID 390874152 (POLiS Cluster of Excellence). D.B. and J.A. additionally acknowledge the basic funding provided by the Helmholtz association. M.A. acknowledges funding by the Graduate & Professional Training Center Ulm. Besides, this study contributes to the research performed

within CELEST (Center for Electrochemical Energy Storage Ulm-Karlsruhe).

REFERENCES

(1) Armand, M.; Axmann, P.; Bresser, D.; Copley, M.; Edström, K.; Ekberg, C.; Guyomard, D.; Lestriez, B.; Novák, P.; Petranikova, M.; et al. Lithium-ion batteries - Current state of the art and anticipated developments. *J. Power Sources* **2020**, *479*, 228708.

(2) Marinaro, M.; Bresser, D.; Beyer, E.; Faguy, P.; Hosoi, K.; Li, H.; Sakovica, J.; Amine, K.; Wohlfahrt-Mehrens, M.; Passerini, S. Bringing forward the development of battery cells for automotive applications: Perspective of R&D activities in China, Japan, the EU and the USA. *J. Power Sources* **2020**, *459*, 228073.

(3) Murdock, B. E.; Toghill, K. E.; Tapia Ruiz, N. A. Perspective on the sustainability of cathode materials used in lithiumion batteries. *Adv. Energy Mater.* **2021**, *11* (39), 2102028.

(4) Vranken, T.Critical raw materials in Li-ion batteries, 2021; https://www.innoenergy.com/news-events/critical-raw-materials-in-li-ion-batteries/.

(5) Manjong, N. B.; Bach, V.; Usai, L.; Marinova, S.; Burheim, O. S.; Finkbeiner, M.; Strømman, A. H. A comparative assessment of value chain criticality of lithium-ion battery cells. *Sustainable Materials and Technologies* **2023**, *36*, e00614.

(6) Hwang, J. Y.; Myung, S. T.; Sun, Y. K. Sodium-ion batteries: present and future. *Chem. Soc. Rev.* **2017**, *46* (12), 3529−3614.

(7) Vaalma, C.; Buchholz, D.; Weil, M.; Passerini, S. A cost and resource analysis of sodium-ion batteries. *Nat. Rev. Mater.* **2018**, *3* (4), 18013.

(8) Hasa, I.; Mariyappan, S.; Saurel, D.; Adelhelm, P.; Koposov, A. Y.; Masquelier, C.; Croguennec, L.; Casas-Cabanas, M. Challenges of today for Na-based batteries of the future: From materials to cell metrics. *J. Power Sources* **2021**, *482*, 228872.

(9) Lu, Y.; Chen, J. Prospects of organic electrode materials for practical lithium batteries. *Nature Reviews Chemistry* **2020**, *4* (3), 127−142.

(10) Chen, H.; Armand, M.; Demailly, G.; Dolhem, F.; Poizot, P.; Tarascon, J. M. From biomass to a renewable LixC6O6 organic electrode for sustainable Li-ion batteries. *ChemSusChem* **2008**, *1* (4), 348−355.

(11) Friebe, C.; Lex-Balducci, A.; Schubert, U. S. Sustainable energy storage: Recent trends and developments toward fully organic batteries. *ChemSusChem* **2019**, *12* (18), 4093−4115.

(12) Janoschka, T.; Hager, M. D.; Schubert, U. S. Powering up the future: radical polymers for battery applications. *Adv. Mater.* **2012**, *24* (48), 6397−6409.

(13) Nakahara, K.; Iwasa, S.; Satoh, M.; Morioka, Y.; Iriyama, J.; Suguro, M.; Hasegawa, E. Rechargeable batteries with organic radical cathodes. *Chem. Phys. Lett.* **2002**, *359* (5), 351−354.

(14) Nishide, H.; Iwasa, S.; Pu, Y.-J.; Suga, T.; Nakahara, K.; Satoh, M. Organic radical battery: nitroxide polymers as a cathode-active material. *Electrochim. Acta* **2004**, *50* (2), 827−831.

(15) Nakahara, K.; Iriyama, J.; Iwasa, S.; Suguro, M.; Satoh, M.; Cairns, E. J. Al-laminated film packaged organic radical battery for high-power applications. *J. Power Sources* **2007**, *163* (2), 1110−1113.

(16) Bugnon, L.; Morton, C. J. H.; Novak, P.; Vetter, J.; Nesvadba, P. Synthesis of poly(4-methacryloyloxy-TEMPO) via group-transfer polymerization and its evaluation in organic radical battery. *Chem. Mater.* **2007**, *19* (11), 2910−2914.

(17) Kim, J.-K.; Kim, Y.; Park, S.; Ko, H.; Kim, Y. Encapsulation of organic active materials in carbon nanotubes for application to high-electrochemical-performance sodium batteries. *Energy Environ. Sci.* **2016**, *9* (4), 1264−1269.

(18) Wang, S.; Park, A. M. G.; Flouda, P.; Easley, A. D.; Li, F.; Ma, T.; Fuchs, G. D.; Lutkenhaus, J. L. Solution-processable thermally crosslinked organic radical polymer battery cathodes. *ChemSusChem* **2020**, *13* (9), 2371−2378.

(19) Suga, T.; Konishi, H.; Nishide, H. Photocrosslinked nitroxide polymer cathode-active materials for application in an organic-based paper battery. *Chem. Commun. (Camb)* **2007**, No. 17, 1730−1732.

(20) Vlad, A.; Rolland, J.; Hauffman, G.; Ernould, B.; Gohy, J. F. Melt-polymerization of TEMPO methacrylates with nano carbons enables superior battery materials. *ChemSusChem* **2015**, *8* (10), 1692−1696.

(21) Iwasa, S.; Nishi, T.; Sato, H.; Nakamura, S. Flexibility and high-rate discharge properties of organic radical batteries with gel-state electrodes. *J. Electrochem. Soc.* **2017**, *164* (4), A884−A888.

(22) Stoyan, D.; Kendall, W. S.; Chiu, S. N.; Mecke, J. *Stochastic Geometry and its Applications*; John Wiley & Sons: 2013.

(23) Jeulin, D. *Morphological Models of Random Structures*; Springer: 2021.

(24) Stenzel, O.; Pecho, O.; Holzer, L.; Neumann, M.; Schmidt, V. Big data for microstructure-property relationships: A case study of predicting effective conductivities. *AIChE J.* **2017**, *63* (9), 4224−4232.

(25) Neumann, M.; Stenzel, O.; Willot, F.; Holzer, L.; Schmidt, V. Quantifying the influence of microstructure on effective conductivity and permeability: Virtual materials testing. *International Journal of Solids and Structures* **2020**, *184*, 211−220.

(26) Wagner, A. C.; Bohn, N.; Geßwein, H.; Neumann, M.; Osenberg, M.; Hilger, A.; Manke, I.; Schmidt, V.; Binder, J. R. Hierarchical structuring of NMC111-cathode materials in lithium-ion batteries: An in-depth study on the influence of primary and secondary particle sizes on electrochemical performance. *ACS Appl. Energy Mater.* **2020**, *3* (12), 12565−12574.

(27) Su, Z.; Decencière, E.; Nguyen, T.-T.; El-Amiry, K.; De Andrade, V.; Franco, A. A.; Demortière, A. Artificial neural network approach for multiphase segmentation of battery electrode nano-CT images. *npj Computational Materials* **2022**, *8* (1), 30.

(28) Furat, O.; Finegan, D. P.; Diercks, D.; Usseglio-Viretta, F.; Smith, K.; Schmidt, V. Mapping the architecture of single lithium ion electrode particles in 3D, using electron backscatter diffraction and machine learning segmentation. *J. Power Sources* **2021**, *483*, 229148.

(29) Cadiou, F.; Douillard, T.; Besnard, N.; Lestriez, B.; Maire, E. Multiscale characterization of composite electrode microstructures for high density lithium-ion batteries guided by the specificities of their electronic and ionic transport mechanisms. *J. Electrochem. Soc.* **2020**, *167* (10), 100521.

(30) Neumann, M.; Ademmer, M.; Osenberg, M.; Hilger, A.; Wilde, F.; Muench, S.; Hager, M. D.; Schubert, U. S.; Manke, I.; Schmidt, V. 3D microstructure characterization of polymer battery electrodes by statistical image analysis based on synchrotron X-ray tomography. *J. Power Sources* **2022**, *542*, 231783.

(31) Tang, F.; Wu, Z.; Yang, C.; Osenberg, M.; Hilger, A.; Dong, K.; Markötter, H.; Manke, I.; Sun, F.; Chen, L.; et al. Synchrotron X-ray tomography for rechargeable battery research: Fundamentals, setups and applications. *Small Methods* **2021**, *5* (9), 2100557.

(32) Heenan, T. M. M.; Tan, C.; Hack, J.; Brett, D. J. L.; Shearing, P. R. Developments in X-ray tomography characterization for electrochemical devices. *Mater. Today* **2019**, *31*, 69−85.

(33) Berg, S.; Kutra, D.; Kroeger, T.; Straehle, C. N.; Kausler, B. X.; Haubold, C.; Schiegg, M.; Ales, J.; Beier, T.; Rudy, M.; et al. ilastik: interactive machine learning for (bio)image analysis. *Nat. Methods* **2019**, *16* (12), 1226−1232.

(34) Wilde, F.; Ogurreck, M.; Greving, I.; Hammel, J. U.; Beckmann, F.; Hipp, A.; Lottermoser, L.; Khokhriakov, I.; Lytaev, P.; Dose, T.; et al. Micro-CT at the imaging beamline P05 at PETRA III. *AIP Conf. Proc.* **2016**, *1741* (1), 030035.

(35) Moosmann, J.; Ershov, A.; Weinhardt, V.; Baumbach, T.; Prasad, M. S.; LaBonne, C.; Xiao, X.; Kashef, J.; Hofmann, R. Time-lapse X-ray phase-contrast microtomography for in vivo imaging and analysis of morphogenesis. *Nat. Protoc.* **2014**, *9* (2), 294−304.

(36) Rudin, L. I.; Osher, S.; Fatemi, E. Nonlinear total variation based noise removal algorithms. *Physica D: Nonlinear Phenomena* **1992**, *60* (1), 259−268.

(37) Westhoff, D.; Danner, T.; Hein, S.; Scurtu, R.; Kremer, L.; Hoffmann, A.; Hilger, A.; Manke, I.; Wohlfahrt-Mehrens, M.; Latz, A.; et al. Analysis of microstructural effects in multi-layer lithium-ion battery cathodes. *Mater. Charact.* **2019**, *151*, 166−174.

(38) Jähne, B. *Digital Image Processing*, 6th ed.; Springer: 2005; pp 350−351.
(39) Tin Kam, H.Random decision forests. In *Proceedings of 3rd International Conference on Document Analysis and Recognition, 14−16 Aug, 1995*; 1995; Vol. *1*, pp 278−282; Vol. 271.
(40) Machado Charry, E.; Neumann, M.; Lahti, J.; Schennach, R.; Schmidt, V.; Zojer, K. Pore space extraction and characterization of sack paper using μ-CT. *J. Microsc.* **2018**, *272* (1), 35−46.
(41) Neumann, M.; Machado Charry, E.; Zojer, K.; Schmidt, V. On variability and interdependence of local porosity and local tortuosity in porous materials: A case study for sack paper. *Methodology and Computing in Applied Probability* **2021**, *23* (2), 613−627.
(42) Schladitz, K.; Ohser, J.; Nagel, W.Measuring intrinsic volumes in digital 3D images. In *Discrete Geometry for Computer Imagery: 13th International Conference, DGCI 2006, Szeged, Hungary, Oct 25−27, 2006, Proceedings 13*; Springer: 2006; pp 247−258.
(43) Neumann, M.; Hirsch, C.; Staněk, J.; Beneš, V.; Schmidt, V. Estimation of geodesic tortuosity and constrictivity in stationary random closed sets. *Scandinavian Journal of Statistics* **2019**, *46* (3), 848−884.
(44) Patra, J.; Rath, P. C.; Yang, C. H.; Saikia, D.; Kao, H. M.; Chang, J. K. Three-dimensional interpenetrating mesoporous carbon confining SnO(2) particles for superior sodiation/desodiation properties. *Nanoscale* **2017**, *9* (25), 8674−8683.
(45) Li, C.; Rath, P. C.; Lu, S.-X.; Patra, J.; Su, C.-Y.; Bresser, D.; Passerini, S.; Chang, J.-K. Ordered nano-structured mesoporous CMK-8 and other carbonaceous positive electrodes for rechargeable aluminum batteries. *Chem. Eng. J.* **2021**, *417*, 129131.
(46) Adhitama, E.; Rath, P. C.; Prayogi, A.; Patra, J.; Lee, T.-C.; Li, J.; Chang, J.-K. High-voltage lithium-metal battery with three-dimensional mesoporous carbon anode host and ether/carbonate binary electrolyte. *Carbon* **2021**, *184*, 752−763.